

Objective Finite-Time Flow Topology from Flowmap Expansion and Contraction

Roxana Bujack¹, Soumya Dutta¹, Duan Zhang¹, and Tobias Günther²

¹ Los Alamos National Laboratory, United States

²Department of Computer Science, ETH Zürich, Switzerland

Abstract. We extend the definition of the classic instantaneous vector field saddles, sinks, and sources to the finite-time setting by categorizing the domain based on the behavior of the flow map w.r.t. contraction or expansion. Since the intuitive Lagrangian approach turns out to be unusable in practice because it requires advection in unstable regions, we provide an alternative, sufficient criterion that can be computed in a robust way. We show that both definitions are objective, relate them to existing approaches, and show how the generalized critical points and their separatrices can be visualized.

Keywords: flow, topology, objectivity, time-dependent, finite-time

1 Introduction

The topological analysis of time-dependent vector fields remains to this day a very active research area in flow visualization. Similar to the classic steady case, we expect that particle motion is guided by a number of topological elements that have mainly been investigated individually, such as vortices [56, 15, 19], separating structures [21, 54, 37] and attractors [59]. In this paper, we introduce a finite-time generalization of the classic 2D vector field topology that maintains physical meaning in time-varying flows. In particular, we request the following properties for the topological structures to be meaningful over finite-time windows:

- In steady flows, the method is consistent with classic vector field topology.
- The definition of topological elements is objective, i.e. invariant w.r.t. Galilean transformations of the frame of reference.
- The feature definition is pathline-oriented and therefore in accordance with particle movement.

In a nutshell, the contributions of this work are as follows

- A coherent theoretical framework of an objective Lagrangian finite-time flow topology that ties together approaches from the literature.
- A non-Lagrangian sufficient definition that exceeds its Lagrangian counterpart in robustness.
- A simple algorithm for the extraction based on first-order approximation.

- Efficient visualizations of the finite-time topology.

Reviewing related work (Section 2), suggests a Lagrangian definition of finite-time topology as a logical consequence, because it bridges the gap between several approaches. Unfortunately, we will see quickly that it is practically useless because of its lack of robustness (Section 3). Therefore, we will dedicate most of this paper to the theoretical analysis of a non-Lagrangian alternative, which forms a sufficient criterion for the intuitive Lagrangian definition (Section 4). Finally, we will showcase results and suggest visualizations.

2 Related Work

Classic Steady Vector Field Topology. Classic steady vector field topology provides us with a compact description of the asymptotic motion of particles [41, 25]. Governing the asymptotic motion are a number of topological elements, which were described by Helman and Hesselink [26], including critical points (sinks, sources, centers, saddles), boundary elements (attachment and detachment points), the manifolds that separate flow regions of homogeneous asymptotic behavior (separatrices), and periodic orbits [2]. The extension to the 3D case [27] gave rise to a broader variety of elements, such as bifurcation lines [39] (lines to which nearby streamlines are asymptotically drawn to or repelled away from at an exponential rate) or saddle connectors [52] (individual streamlines that connect saddles). Aside from characterizations as extremal lines [32] of vortex-related scalar fields [46, 47], vortex corelines have also been expressed as lines along which the velocity vector aligns with the single real-valued eigenvector of the Jacobian matrix [51]. The parallel vectors operator [38] became a very powerful descriptor for such line features. In fact, both vortex corelines and bifurcation lines can be expressed in this way, with the only difference being that vortex corelines require swirling motion [38] (complex eigenvalues in the Jacobian) and bifurcation lines require attracting and repelling behavior [43, 37] (negative determinant in the plane orthogonal to the flow). Extensions include the characterization of higher-order critical points into sectors of elliptic, parabolic, or hyperbolic behavior [48, 7, 58] and higher-order bent vortex corelines [44].

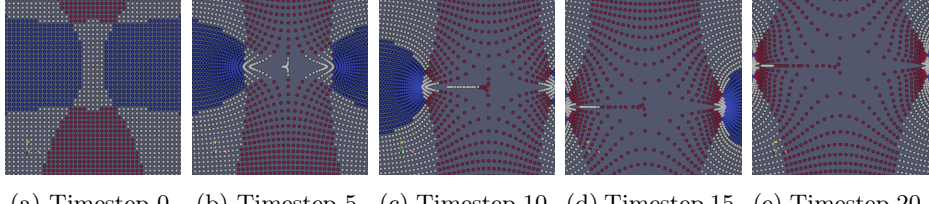
Streamlines vs. Pathlines. More recent research concentrated on the definition and extraction of topological structures in time-dependent flows [40], in which we face two major challenges. First, aside from periodic flows, the temporal domain is usually bounded, which does not permit the observation of asymptotic motion. Second, the topology of streamlines (i.e., the observation of individual time slices) is irrelevant for pathlines, which was for instance demonstrated for vortex corelines [56]. The difference between streamline-oriented and pathline-oriented topology was discussed by Theisel et al. [53] in detail. Wiebel et al. [59] demonstrated in a simple 2D rotating petri-dish example that most existing techniques fail to detect the attracting vortex center that moves on a circular path. In the literature, this flow is sometimes also referred to as the Beads

problem [57]. Integration-based methods can find the coreline, including the particle density estimate to extract the preferential particle settling [59] and the vortex coreline in the vector field in which streaklines are tangent curves [57]. Local methods failed due to lack of rotation invariance in the feature definitions, which can be obtained by a deformation from Cartesian to polar coordinates [17].

Reference Frames. A number of methods suggest to reduce the time-dependent topology back to the steady case by a suitable choice of the reference frame. Wiebel et al. [60] and Bhatia et al. [3] used flow decompositions to subtract a flow component that is irrotational and incompressible, i.e., harmonic. Fuchs et al. [13] selected a reference frame in which the velocity vanishes at locations at which the acceleration is zero. Bujack et al. [5] selected extrema in the determinant of the Jacobian to determine the reference frame. To determine a reference frame in which the vector field becomes steady [36, 42], reference frames have been calculated by local [15, 18] and global [19] linear optimizations, as well as by deep learning [31]. Alternatively, several local feature definitions possess a certain reference frame invariance. However, most of them, are only invariant to equal-speed translations, e.g., vorticity, λ_2 [29], and the Q -criterion [28]. Objectivity is achieved only by a few, such as by the instantaneous vorticity deviation [23].

Lagrangian Coherent Structures. In contrast to the local approaches, a large body of research searched for structures that behave coherently over a finite-time window. This research includes region-based vortex methods [23], coherent sets [12], and coherent line and surface structures, typically called Lagrangian coherent structures (LCS) [22]. The latter results in material lines that order the flow, including jet cores (parabolic LCS), vortex boundaries (elliptic LCS) and separating structures (hyperbolic LCS). As approximation to hyperbolic LCS, Haller [24] suggested to use the finite-time Lyapunov exponent (FTLE) [49], which measures the separation of nearby-released particles over a finite-time window. A number of approaches to compute FTLE exist, including a discretization of the flow map [24], localized FTLE [30], timeline cell tracking [33], a direct sampling of an advected circle [55] and Monte Carlo rendering [16]. Later, Haller [21] suggested to extract hyperbolic LCS by looking for the biggest separation orthogonal to a material surface. Similarly, Friederici et al. [11, 10] analyzed the finite-time separation orthogonal to a separatrix in steady flows.

Time-dependent Saddles. Theisel et al. [53] categorized pathlines into attractors, repellors, and saddle-like trajectories based on whether their surrounding pathlines converge toward it in forward integration, in backward integration, or neither. In the fluid dynamics community, Haller [20] defined uniformly hyperbolic trajectories as pathlines with the property that half of their neighboring pathlines converge toward them in forward direction and the other in backward direction. Further, he introduced the concept of hyperbolicity time as the maximal amount of time a pathline spends in a region in which the Jacobian determinant is strictly negative and shows that the local maxima of hyperbolicity



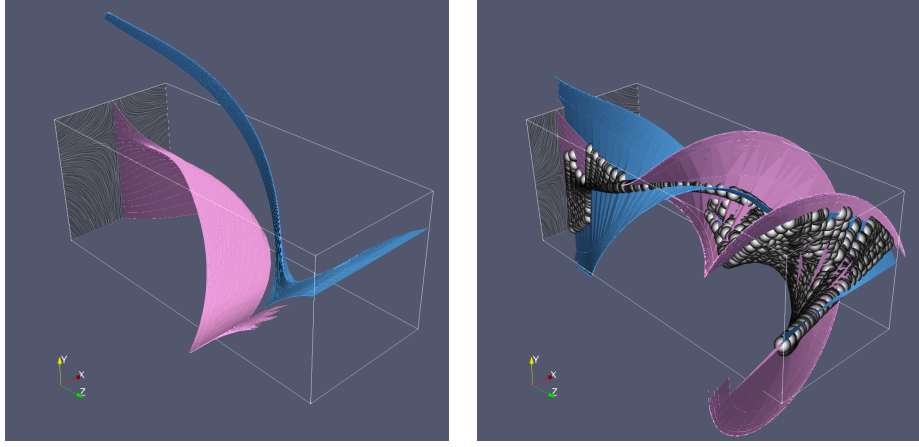
(a) Timestep 0. (b) Timestep 5. (c) Timestep 10. (d) Timestep 15. (e) Timestep 20.

Fig. 1: The Lagrangian definition is not robust. Categorization of the pathlines of the accelerated translation of a steady saddle is visualized through color coding: red—source; blue—sink; white—saddle. Theoretically, the saddle in the center of timestep 0 should move once around on a circle around the origin of coordinates. Instead it is fully driven away by the expanding regions.

time are a first approximation to the uniformly hyperbolic trajectories. Inspired by Haller’s hyperbolic trajectories [20], Sadlo and Weiskopf [45] generalized the concept of saddle-type critical points to time-dependent vector fields using the intersections of forward and backward FTLE ridges. The motivation behind this choice is that just like saddles, these areas show divergent behavior in forward as well as backward direction in time. As introduced by Wiebel et al. [61], they used these points as seeds for generalized streaklines, which form a generalization of separatrices to time-dependent flows. Later, Üffinger et al. [54] extended the concept to 3D. To approximate the path of a saddle, i.e., a bifurcation line in 2D space-time, Machado et al. [37] applied the reduced velocity criterion [51, 38] and iteratively aligned the extracted bifurcation line with the flow to obtain a pathline. In his recent survey on LCS, Haller [22] formulated four desirable properties: objectivity, finite-time nature, Lagrangian invariance, and spatial convergence. He points out that most classic definitions of material stability look strictly in forward direction to assess repelling behavior and strictly in backward direction to assess repelling behavior. Instead, repelling and attracting behavior should be assessed over the full time window, i.e., both forward and backward from the current point in time. He rejected Shadden’s definition of LCS as second derivative ridges [49] and suggests shrink lines and stretch lines as LCSs [8, 9].

3 Intuitive Approach

Many attempts to generalize classic vector field topology to a time-dependent setting are based on translating the convergence and divergence properties of the classic critical points to pathlines. Most approaches deal with saddles [45, 20, 21, 4]. A few take into account sources or sinks, too [53, 59]. In this paper, we also base our categorization on that pulling together existing work into one coherent framework. Intuitively speaking, we consider a pathline a **Lagrangian finite-time saddle** if part of its neighborhood has attracting behavior and part of its neighborhood has repelling behavior. We consider it a **Lagrangian finite-time sink** if all of its neighborhood has attracting behavior, and a **Lagrangian**



(a) FTLE ridges for the saddle under accelerated translation do not intersect. (b) They intersect almost everywhere for the saddle under accelerated translation.

Fig. 2: Lagrangian intersection of forward and backward FTLE is not robust.

finite-time source if all of its neighborhood has repelling behavior. The term Lagrangian or Lagrangian invariant refers to the ability of a structure to move with the flow, i.e. to be invariant w.r.t. advection [22]. We translate this into a concise mathematical definition.

Definition 1 (Lagrangian Finite-time Topological Categories) *We consider a point and time $(x_0, t) \in \mathbb{R}^d \times \mathbb{R}$ a Lagrangian finite-time saddle for a given time interval $t \in [t_0, t_1] \subset \mathbb{R}$ if for any $\epsilon > 0$, we can find a plane containing 4 points $x_1, \dots, x_4 \in B_\epsilon(x_0)$ in its ϵ -neighborhood (numbered in positive orientation around x_0) so that the pathlines starting at (x_1, t) and (x_3, t) will expand from x_0 forward in time until t_1 while (x_2, t) and (x_4, t) contract. We consider it a Lagrangian finite-time sink if there is an $\epsilon_0 > 0$ such that for all $\epsilon : \epsilon_0 > \epsilon > 0$, a pathline starting at any point $x \in B_\epsilon(x_0)$ in its ϵ -neighborhood will contract to x_0 and a finite-time source if it expands.*

To categorize the steady flow behavior in finite-time, we define contraction and expansion as follows:

Definition 2 (Finite-time Contraction and Expansion) *We consider two trajectories $x_0(t), x_i(t) : \mathbb{R} \rightarrow \mathbb{R}^d$ expanding in forward time for a given finite-time interval $t \in [t_0, t_1]$ if $\|x_0(t_0) - x_i(t_0)\| < \|x_0(t_1) - x_i(t_1)\|$ and contracting if $\|x_0(t_0) - x_i(t_0)\| > \|x_0(t_1) - x_i(t_1)\|$. Expansion in forward time is equivalent to contraction in backward time and vice versa.*

Definition 1 is objective [50] and Lagrangian invariant [22], i.e. it is advected by the flow. It is not able to classify centers and it does not always coincide with the steady topology, for example for linear fields. It is straightforward and very intuitive and nicely ties together different related work, but it suffers from

a significant drawback. In practice, it is pretty much unusable because it is not robust. The categorization of the different pathlines at time t_0 works just fine, but to determine where these areas of a category go, we have to integrate along unstable manifolds that strongly deflect the pathlines, Figure 1.

Impossibility of integration purely along stable manifolds. To advect in a robust way, an idea would be to make use of the backward integration [45, 20, 21]. But advecting forward the forward time attracting regions (sinks and part of the saddles) and advecting backward time attracting regions (sources and the other part of the saddles) backward in time does not work either, because the saddle lies on a repelling manifold for both directions. This part will be deflected no matter from where we integrate. Figure 2 illustrates the problem in space-time. Theoretically, the saddle lies on the intersection line of the attracting manifolds in forward and backward direction. But due to the strong deflection, the surfaces may not intersect at all or become aligned.

4 Theory

In this section, we will provide a definition of a non-Lagrangian finite-time topology, which is a necessary condition for the intuitive Definition 1, but allows for a robust extraction. We will study its properties and derive an algorithm for its efficient computation based on its first-order approximation.

4.1 Mathematical Definition

Analogously to the Lagrangian Definition 1, we state a concise mathematical definition that concisely describes the intuitive physical categorization of the domain into contracting and expanding regions. The first of the two main differences is that we no longer require these regions to be Lagrangian, which means that instead of categorizing pathlines, we categorize points in space and time. Second, we explicitly consider these point's contracting and expanding behavior (Definition 2) in forward and also in backward time.

Definition 3 (Finite-time Topological Categories) *We consider a point in space and time $(x_0, t) \in \mathbb{R}^d \times \mathbb{R}$ a **finite-time saddle** for a given time interval $t \in [t_0, t_1] \subset \mathbb{R}$ if for any $\epsilon > 0$, we can find 4 points $x_1, \dots, x_4 \in B_\epsilon(x_0)$ in its ϵ -neighborhood (numbered in positive orientation around x_0) so that the pathlines starting at (x_1, t) and (x_3, t) will expand from x_0 forward in time until t_1 and contract backward until t_0 while (x_2, t) and (x_4, t) do the opposite. We consider it a **finite-time sink** if there is an $\epsilon_0 > 0$ such that all $\epsilon : \epsilon_0 > \epsilon > 0$, so that a pathline starting at any point $x \in B_\epsilon(x_0)$ in its ϵ -neighborhood will contract to x_0 forward in time until t_1 and expands backward until t_0 and a **finite-time source** for the opposite.*

4.2 Relation to the Lagrangian Definition

Definition 3 is sufficient for Definition 1, which means that every point in space and time that is classified as a finite-time saddle/source/sink lies on a pathline that is classified as a Lagrangian finite-time saddle/source/sink.

To see that, let

$$F_{t_0}^{t_1} : \mathbb{R} \times \mathbb{R} \times \mathbb{R}^d \rightarrow \mathbb{R}^d, \quad t \times t_0 \times x_0 \mapsto F_{t_0}^{t_1}(x_0), \quad (1)$$

with

$$\begin{aligned} F_{t_0}^{t_0}(x_0) &= x_0, \\ F_{t_1}^{t_2}(F_{t_0}^{t_1}(x_0)) &= F_{t_0}^{t_2}(x_0), \end{aligned} \quad (2)$$

denote the flow map describing how a flow parcel at (x_0, t_0) moves to $F_{t_0}^{t_1}(x_0)$ in the time interval $t_1 - t_0$. Then, we can compactly write the conditions in Definition 3. For a saddle, there exist x_{odd}, x_{even} such that:

$$\begin{aligned} \|F_t^{t_1}(x_{odd}) - F_t^{t_1}(x_0)\| &> \|x_{odd} - x_0\|, \\ \|F_t^{t_1}(x_{even}) - F_t^{t_1}(x_0)\| &< \|x_{even} - x_0\|, \\ \|F_t^{t_0}(x_{odd}) - F_t^{t_0}(x_0)\| &< \|x_{odd} - x_0\|, \\ \|F_t^{t_0}(x_{even}) - F_t^{t_0}(x_0)\| &> \|x_{even} - x_0\|, \end{aligned} \quad (3)$$

for a sink for all x_i holds:

$$\begin{aligned} \|F_t^{t_1}(x_i) - F_t^{t_1}(x_0)\| &< \|x_i - x_0\|, \\ \|F_t^{t_0}(x_i) - F_t^{t_0}(x_0)\| &> \|x_i - x_0\|, \end{aligned} \quad (4)$$

and for a source for all x_i holds:

$$\begin{aligned} \|F_t^{t_1}(x_i) - F_t^{t_1}(x_0)\| &> \|x_i - x_0\|, \\ \|F_t^{t_0}(x_i) - F_t^{t_0}(x_0)\| &< \|x_i - x_0\|. \end{aligned} \quad (5)$$

From this, we can directly derive the properties of the pathline through (x_0, t) . We will show this for the case of a source. Assume (5) holds then at time t_0 , all points $(F_t^{t_0}(x_i), t_0)$ in the neighborhood of the starting location of this pathline $(F_t^{t_0}(x_0), t_0)$ satisfy

$$\|F_t^{t_0}(x_i) - F_t^{t_0}(x_0)\| \stackrel{(5)}{<} \|x_i - x_0\| \stackrel{(5)}{<} \|F_t^{t_1}(x_i) - F_t^{t_1}(x_0)\|, \quad (6)$$

which is the condition for the pathline to be a Lagrangian finite-time source. The size of ϵ_0 in Definition 1 depends on the respective flow field, but its existence is guaranteed if it is continuous, because the flowmap is as many times differentiable as the vector field [1]. The other cases work analogously.

4.3 Objectivity

We consider objectivity [50] important because this property ensures that two observers do not get different answers from looking at the same physical phenomenon. Within the flow, smaller features get advected by larger ones, which results as a mixture of different 'best' reference frames to look at the flow. Definition 3 is objective, i.e. invariant w.r.t a Euclidean transformation of the reference frame $x' = Q(t)x + c(t)$ with a time-dependent orthogonal matrix $Q : \mathbb{R} \rightarrow SO(d)$ and a translation $c : \mathbb{R} \rightarrow \mathbb{R}^d$. This follows from the transformation properties of the flowmap under Euclidean transformations $F'^{t_1}_{t_0}(x'_0) = Q(t_1)F^{t_1}_{t_0}(x_0) - c(t_1)$ [35], because of which the difference suffices

$$\begin{aligned} F'^{t_1}_{t_0}(x'_0) - F'^{t_1}_t(x'_i) &= Q(t_1)F^{t_1}_{t_0}(x_0) - c(t_1) - Q(t_1)F^{t_1}_t(x_i) + c(t_1) \\ &= Q(t_1)(F^{t_1}_{t_0}(x_0) - F^{t_1}_t(x_i)) \end{aligned} \quad (7)$$

and the distance

$$\begin{aligned} \|F'^{t_1}_{t_0}(x'_0) - F'^{t_1}_t(x'_i)\|^2 &= (F'^{t_1}_{t_0}(x'_0) - F'^{t_1}_t(x'_i))^T(F'^{t_1}_{t_0}(x'_0) - F'^{t_1}_t(x'_i)) \\ &\stackrel{(7)}{=} (Q(t_1)(F^{t_1}_{t_0}(x_0) - F^{t_1}_t(x_i)))^T(Q(t_1)(F^{t_1}_{t_0}(x_0) - F^{t_1}_t(x_i))) \\ &= (F^{t_1}_{t_0}(x_0) - F^{t_1}_t(x_i))^T Q(t_1)^T Q(t_1)(F^{t_1}_{t_0}(x_0) - F^{t_1}_t(x_i)) \\ &= (F^{t_1}_{t_0}(x_0) - F^{t_1}_t(x_i))^T(F^{t_1}_{t_0}(x_0) - F^{t_1}_t(x_i)) \\ &= \|F^{t_1}_{t_0}(x_0) - F^{t_1}_t(x_i)\|. \end{aligned} \quad (8)$$

4.4 Linear Approximation

The difference between two close points can be approximated using Taylor's theorem. In our case, the conditions (3) to (5) can be expressed using the deformation gradient $\nabla F : \mathbb{R}^{d \times d}$

$$F^{t_1}_t(x_0) - F^{t_1}_t(x_i) = \nabla F^{t_1}_t(x_0)(x_i - x_0) + O(\|x_i - x_0\|^2). \quad (9)$$

For the limit $\epsilon \rightarrow 0$, we can write its magnitude as

$$\begin{aligned} \|F^{t_1}_t(x_0) - F^{t_1}_t(x_i)\|^2 &= (F^{t_1}_t(x_0) - F^{t_1}_t(x_i))^T(F^{t_1}_t(x_0) - F^{t_1}_t(x_i)) \\ &= (x_0 - x_i)^T(\nabla F^{t_1}_t(x_0))^T \nabla F^{t_1}_t(x_0)(x_0 - x_i). \end{aligned} \quad (10)$$

The first part of condition (5) can be rewritten as the ratio

$$\frac{\|F^{t_1}_t(x_0) - F^{t_1}_t(x_i)\|}{\|x_0 - x_i\|} > 1. \quad (11)$$

With the unit vector

$$n = \frac{x_0 - x_i}{\|x_0 - x_i\|} \quad (12)$$

and the Cauchy-Green strain tensor $C_{t_0}^{t_1}(x_0) = (\nabla F_{t_0}^{t_1}(x_0))^T \nabla F_{t_0}^{t_1}(x_0)$ from continuum mechanics, the ratio (11) can be estimated through

$$\frac{\|F_t^{t_1}(x_0) - F_t^{t_1}(x_i)\|^2}{\|x_0 - x_i\|^2} = n^T (\nabla F_t^{t_1}(x_0))^T \nabla F_t^{t_1}(x_0) n = n^T C_t^{t_1}(x_0) n. \quad (13)$$

Because of

$$\frac{\|F_t^{t_1}(x_1) - F_t^{t_1}(x_3)\|}{\|x_1 - x_3\|} > 1 \Leftrightarrow \frac{\|F_t^{t_1}(x_1) - F_t^{t_1}(x_3)\|^2}{\|x_1 - x_3\|^2} > 1 \Leftrightarrow n^T C_t^{t_1}(x_0) n > 1, \quad (14)$$

the conditions in (3) to (5) can be expressed through the eigenvalues of C . Since the eigenvectors maximize $\max_{\|n\|=1} |n^T C n|$, the conditions are transferred to the eigenvalues. In particular, for a point (x_0, t) to be a first-order approximation to the finite-time saddle in the interval $[t_0, t_1]$, the tensors $C_t^{t_1}(x_0)$ and $C_t^{t_0}(x_0)$ must each have eigenvalues greater as well as smaller than 1. The eigenvalues need to be both smaller than 1 for $C_t^{t_1}(x_0)$ and both greater than 1 for $C_t^{t_0}(x_0)$ for a point to be a first-order approximation of a finite-time sink and the opposite for a finite-time source.

The linear approximation is also objective. Because of $\nabla_{x'} x = \frac{d x}{d x'} = Q^T$ and the chain rule [35], the deformation gradient suffices:

$$\nabla F_{t_0}^{t_1'}(x') = Q(t_1) \nabla F_{t_0}^{t_1}(x) Q(t_0)^T. \quad (15)$$

and the Cauchy-Green strain tensor

$$\begin{aligned} C_{t_0}^{t_1'}(x') &= (\nabla F_{t_0}^{t_1'}(x'))^T \nabla F_{t_0}^{t_1'}(x') \\ &= (Q(t_1) \nabla F_{t_0}^{t_1}(x) Q(t_0)^T)^T Q(t_1) \nabla F_{t_0}^{t_1}(x) Q(t_0)^T \\ &= Q(t_0)((\nabla F_{t_0}^{t_1}(x))^T \nabla F_{t_0}^{t_1}(x)) Q(t_0)^T \\ &= Q(t_0) C_{t_0}^{t_1}(x) Q(t_0)^T. \end{aligned} \quad (16)$$

This approximation is not necessarily objective, because it has two time dependencies that the definition of objectivity does not encompass, but its eigenvalues are objective. Let v be an eigenvector of C' with eigenvalue λ , i.e. $Cv = \lambda v$, then $\tilde{v} = Q(t_0)v$ is an eigenvector of C with the same eigenvalue

$$C' \tilde{v} \stackrel{(16)}{=} Q(t_0) C_{t_0}^{t_1}(x) Q(t_0)^T \tilde{v} = Q(t_0) C_{t_0}^{t_1}(x) v = Q(t_0) \lambda v = \lambda Q(t_0) v = \lambda \tilde{v}. \quad (17)$$

4.5 Strength

As can be seen in Figure 1, Definitions 1 and 3 usually do not produce isolated points but areas of coherent classification. For each connected component of one category, we can choose a point as a representative through demanding that it shows the corresponding contracting or expanding behavior in locally the

strongest way, for example for the saddle through maximizing

$$M_{t_0}^{t_1}(x_0, t) := \max_{x_{odd}, x_{even} \in B_\epsilon(x_0)} \min\left(\frac{\|F_t^{t_1}(x_{odd}) - F_t^{t_1}(x_0)\|}{\|x_{odd} - x_0\|}, \frac{\|x_{even} - x_0\|}{\|F_t^{t_1}(x_{even}) - F_t^{t_1}(x_0)\|}, \right. \\ \left. \frac{\|x_{odd} - x_0\|}{\|F_t^{t_0}(x_{odd}) - F_t^{t_0}(x_0)\|}, \frac{\|F_t^{t_0}(x_{even}) - F_t^{t_0}(x_0)\|}{\|x_{even} - x_0\|}\right), \quad (18)$$

for the sink through maximizing

$$M_{t_0}^{t_1}(x_0, t) := \min_{x_i \in B_\epsilon(x_0)} \min\left(\frac{\|F_t^{t_1}(x_i) - F_t^{t_1}(x_0)\|}{\|x_i - x_0\|}, \frac{\|x_i - x_0\|}{\|F_t^{t_0}(x_i) - F_t^{t_0}(x_0)\|}\right), \quad (19)$$

and for the source through maximizing

$$M_{t_0}^{t_1}(x_0, t) := \min_{x_i \in B_\epsilon(x_0)} \min\left(\frac{\|x_i - x_0\|}{\|F_t^{t_1}(x_i) - F_t^{t_1}(x_0)\|}, \frac{\|F_t^{t_0}(x_i) - F_t^{t_0}(x_0)\|}{\|x_i - x_0\|}\right). \quad (20)$$

The inner most min refers to the minimum of the forward and backward terms to avoid the detection of examples that only exhibit the behavior in one direction. The second min avoids line sinks and sources, which do not have expanding or contracting behavior in one direction. The outer most maximization refers to the candidate points x_0 that exhibit the respective behavior in locally the strongest way.

4.6 Weighting Related to FTLE

The first-order approximation shows that our measures of strength are related to FTLE, where the largest eigenvalue λ_{max} of the Cauchy-Green strain tensor C is evaluated. To consider the dependence on the size of the time interval and the potentially rapid growth of the expansion, λ_{max} is weighted via

$$\tilde{\lambda}_{max}(C_{t_0}^{t_1}(x_0)) := FTLE_{t_0}^{t_1}(x_0) = \frac{\log \sqrt{\lambda_{max}(C_{t_0}^{t_1}(x_0))}}{t_1 - t_0}, \quad (21)$$

Analogously, we can weight the largest and smallest eigenvalue $\lambda_{max}, \lambda_{min}$ of the Cauchy-Green strain tensor for weighted first-order approximations of our measures of strength. The logarithm changes the limit where changes between the categories happen to 0, which leads to the following cases

$$(x_0, t) \text{ is a } \begin{cases} \text{saddle} & \text{if } \tilde{\lambda}_{max}(C_t^{t_1}) > 0 \wedge \tilde{\lambda}_{min}(C_t^{t_1}) < 0 \wedge \tilde{\lambda}_{max}(C_t^{t_0}) > 0 \\ & \wedge \tilde{\lambda}_{min}(C_t^{t_0}) < 0 \wedge v_{max}(C_t^{t_1}) \neq v_{min}(C_t^{t_0}), \\ \text{source} & \text{if } \wedge \tilde{\lambda}_{min}(C_t^{t_1}) > 0 \wedge \tilde{\lambda}_{max}(C_t^{t_0}) < 0, \\ \text{sink} & \text{if } \wedge \tilde{\lambda}_{max}(C_t^{t_1}) < 0 \wedge \tilde{\lambda}_{min}(C_t^{t_0}) > 0 \\ \text{neither} & \text{else.} \end{cases} \quad (22)$$

Please note that for a first-order saddle, we additionally have to make sure that the directions of the strongest expansion in forward and backward time do not coincide to guarantee that there are really 4 separate points x_i as demanded in Definition 3 instead of x_{odd} as suggested in forward time to coincide with x_{even} as suggested by backward time, which would occur for example for a blue sky bifurcation, i.e. a flow that is first a sink and then turns into a source or vice versa.

That also means that we can directly use the absolute value of the weighted eigenvalues to determine how strong the contracting or expanding properties of each point are. In particular, we use the minimum over all four $\tilde{\lambda}$

$$\tilde{M}_{t_0}^{t_1}(x_0, t) := \min_{i \in \{0,1\}} \min_{j \in \{min, max\}} \frac{|\tilde{\lambda}_j(C_t^{t_i}(x_0))|}{|t_i - t|}. \quad (23)$$

If a point does not fall into a category (for example, it is a source in forward time and saddle in backward time), we set the strength to zero. If a point is a saddle, we additionally weight it by the scalar product across the eigenvectors to exclude areas where they coincide in forward and backward direction. All in all, we get the measure of strength

$$\mathcal{M}_{t_0}^{t_1}(x_0, t) = \begin{cases} \tilde{M}_{t_0}^{t_1}(x_0, t) & \text{if source or sink,} \\ |v_{max}(C_t^{t_1})^T v_{min}(C_t^{t_0})| \tilde{M}_{t_0}^{t_1}(x_0, t) & \text{if saddle,} \\ 0 & \text{else.} \end{cases} \quad (24)$$

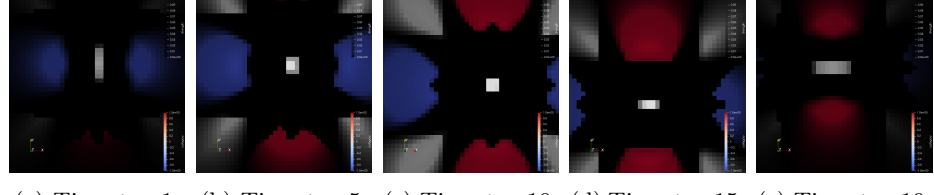
We compute this scalar measure of strength for the whole domain, which will allow us to determine strong representatives for coherent regions of the same behavior and to remove weak occurrences for reducing clutter in the visualizations. Since, the eigenvectors are orthogonal, we do not need to consider the other pair.

The measure of strength is also objective. We already know that the eigenvalues are objective from (17) and we can see that the product of the eigenvectors $v_1(C_t^{t_1}(x_0))^T v_2(C_t^{t_0}(x_0))$ is objective, too, because their transformed equivalents suffice

$$\begin{aligned} v'_1(C_t^{t_1'}(x'_0))^T v'_2(C_t^{t_0'}(x'_0)) &\stackrel{(17)}{=} (Q(t)v_1(C_t^{t_1}(x_0)))^T Q(t)v_2(C_t^{t_0}(x_0)) \\ &= v_1(C_t^{t_1}(x_0))^T v_2(C_t^{t_0}(x_0)). \end{aligned} \quad (25)$$

4.7 Separatrices

It is common practice to use generalized streaklines [61] seeded around the locally strongest saddles, sometimes also called bifurcation lines in space-time, [45, 54, 37]. In particular, we seed pathlines with a small offset in both directions of the eigenvector $v_{max}(C_t^{t_1}(x_0))$ corresponding to the bigger eigenvalue for the forward separatrix advection and analogously with a small offset in both directions of the eigenvector $v_{max}(C_t^{t_0}(x_0))$ for the backward separatrix. Then, we generate surfaces from them in space-time. Figure 5 shows a visualization. The temporally local separatrices can be produced from slicing the volume at one timestep.



(a) Timestep 1. (b) Timestep 5. (c) Timestep 10. (d) Timestep 15. (e) Timestep 19.

Fig. 3: The non-Lagrangian definition correctly categorizes the pathlines of the accelerated translation of a steady saddle. Red: source, blue: sink, white: saddle, black: neither. We show the strength of each region by overlaying (24) ranging from black for low strength to transparent for high strength.

5 Experiments

In this section, we concentrate mainly on experiments for which we actually know the ground truth to demonstrate the correctness of the proposed method. For this purpose, we use two analytic data sets. The first one is a steady saddle

$$v(x) = v(x, y) = 2 \begin{pmatrix} x + 0.5 \\ -y \end{pmatrix} e^{-2\sqrt{(x+0.5)^2+y^2}} \quad (26)$$

that is moved through an accelerated translation. A Euclidean transformation

$$x' = Q(t)x + c(t) \quad (27)$$

changes a velocity field via

$$v'(x, t) = Q(t)v(Q^T(t)(x - c(t))) + \dot{Q}(t)(x - c(t)) + \dot{c}(t). \quad (28)$$

We use $c(t) = \frac{1}{2}(\sin(\theta) + 1, \cos(\theta))^T$ with $\theta = 2\pi t^2/|T|^2$ and $|T|$ denoting the number of time steps, which moves the saddle clockwise on the circle with radius 0.5 around $(0, 0)^T$ starting at $(0, 0.5)^T$. The motivation of using accelerated moving reference frames is that this is the most complicated case. If a method detects this one correctly, it will also work for constant movements. We have already seen the results of the Lagrangian categorization for this dataset in Figure 1. The results of the robust categorization using the suggested sufficient first-order approximation suggested in this work can be found in Figure 3. This figure shows the expected behavior with the accelerated movement around the origin. On top of the category, we also encode the strength of the occurrence fading out weak areas into black. This approach is consistent with color-coding black areas that belong in no category. Please note that the two sources (red) and two sinks (blue) around the saddle (white) are a result of the Gaussian weighting in combination with the saddle. The actual expanding and contracting character of these regions can be well perceived in the particle view Figure 1 offers.

The second analytic dataset is the same saddle (26) performing an accelerated rotation with $Q(t) \in SO_2$ being the rotation matrix by $\theta = 2\pi t^2/|T|^2$. For both

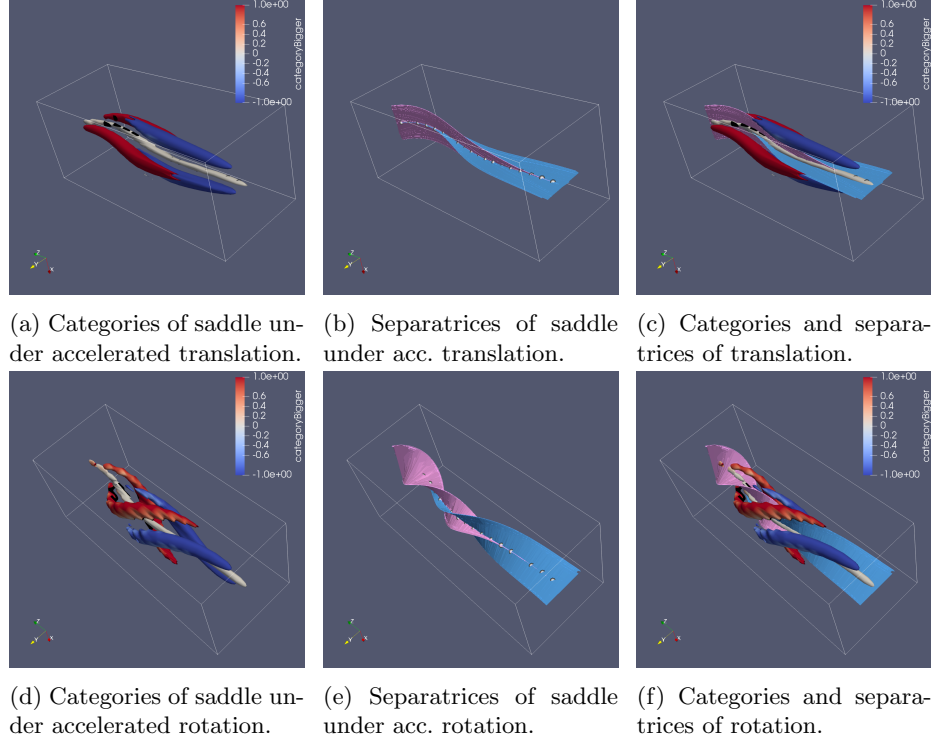


Fig. 4: Visualizations of the finite-time topology in space-time for two examples of Euclidean transformations. Left: isosurfaces of the strength colored by category. Red—source; blue—sink; white—saddle. Middle: separatrices, i.e. streak surfaces forward (red) and backward (blue) in time seeded at the strongest saddle offset in the direction of the eigenvectors of the Cauchy Green strain tensor. Right: both. The path of the saddle is one full circle in both cases. The shapes of the sinks, sources, and separatrices reveal that the top movement is a pure translation, whereas the bottom is a rotation.

flows, we use the spatial domain $[-2, 2]^2$ with resolution 81^2 and the full 21 time steps $[t_1, t_1] = [0, 20]$. To avoid boundary artifacts, we computed the flowmap on a bigger domain. Both transformations are purely Euclidean. They can be interpreted as a change of the reference frame of the observer and an objective method should be able to detect the saddle on the circle.

Figure 4 shows the results of the classification and the separatrices for both transformations in space-time. We visualize the different categories using the same color coding. Saddles are white, sources are red, sinks are blue, and points that fall in no category are black. For the reduction of weak occurrences to gain a less cluttered, more expressive visualization, we applied isocontours on the scalar strength field (24) and colored the result using the scalar field of the categories (22). Storing the two fields makes the visualization of the method

easy in any common visualization tool. To get the separatrices for each time slice, we first chose representatives for the saddle-type regions by selecting the locations with the global maximum of the strength. Then, we seeded pathlines as described in Section 4.7. Our method detects the true locations of the saddle up to the accuracy of one cell. It cannot find the exact location within a cell, because the maximum always lies on a gridpoint in a piecewise linear field.

For these datasets, the intersection of forward and backward FTLE as suggested by Sadlo [45] produces the same results. The Lagrangian forward and backward FTLE produces no result for the detection of the saddles. Even though, the ridges are detected correctly at the first and last time step, the surfaces are deflected so strongly that they do not intersect at all for the translation and almost everywhere for the rotation, Figure 1.

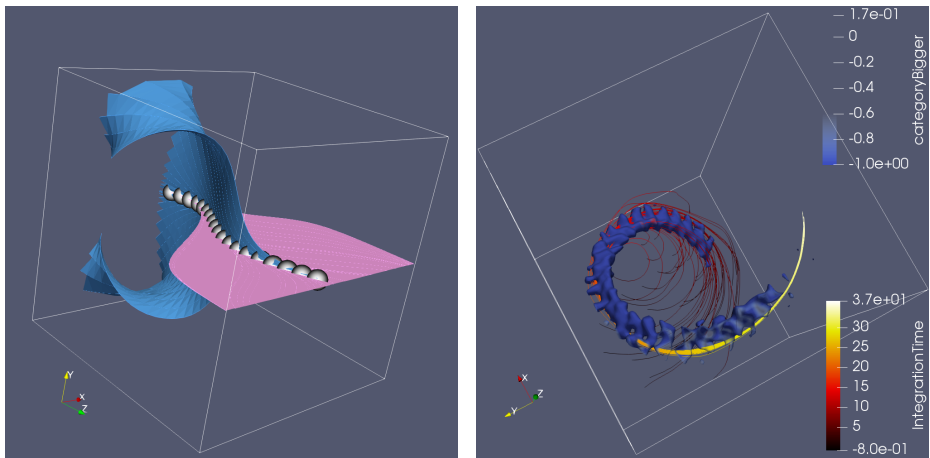
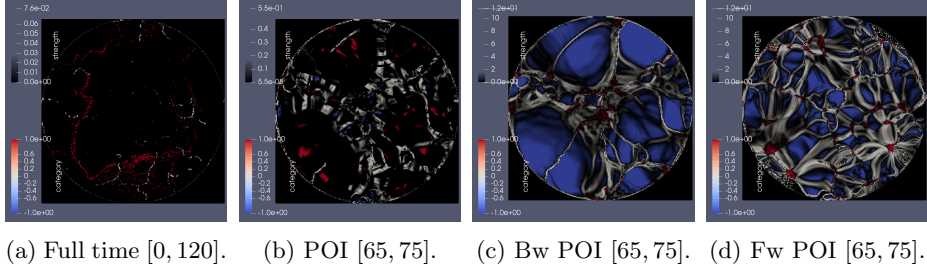


Fig. 5: Quad gyre: separatrices (pink: fw, blue: bw) of strongest saddle in spacetime.

Fig. 6: Petri-dish: the rotating sink (blue) and pathlines for comparison in spacetime.

Figure 5 shows the extraction of the strongest saddle and the separatrices of the quad gyre, which extends the double gyre [49] to the domain $[0, 1]^2$. We used the resolution 201^2 and one full period in time. Here, the global maximum of our measure (24) coincides with the intersection of forward and backward FTLE of the adjacent intervals [45]. The double gyre is an incompressible flow, which is why it does not have sources and sinks.

Figures 6 and 7 show results of the categorization for two flow simulations using red for sources, blue for sinks, white for saddles, and black for neither. The rotating sink in the last 40 timesteps of the petri-dish dataset [6, 59, 5] is nicely extracted but the complicated topology in the viscous fingers dataset [34] from the SciVis contest <http://sciviscontest.ieeevis.org> is harder to interpret. A limit of our method is reached if the data shows strong contraction and spans

Fig. 7: Categorization in viscous fingers dataset for timestep $t = 70$.

a long period of time. Once all particles in the flowmap are accumulated in one point, nothing is left for it to capture in coming time steps, which leads to detail getting lost and most points not belonging in either category 7a. We show the strength of each region by overlaying (24), ranging from black for low strength to transparent for high strength. This issue is a known problem of Lagrangian methods and can be overcome by guaranteeing Lagrangian invariance for a time period of interest (POI) only [14]. Figure 7 top shows the difference of the global $[t_0, t_1] = [0, 120]$ and the POI $[65, 75]$ approach for time step 70. Figure 7 bottom shows the partial POI categories considering only backward and only forward information, which together form Figure 7b. The comparison shows that the chosen time interval influences how a point is categorized.

6 Discussion

The extension of vector field topology to time-dependent flows has been extensively studied not only in the scientific visualization community. Our results are based on many approaches that have been published previously.

The closest related work w.r.t. saddle is [4]. The definition of finite-time saddle is identical to ours, but sources and sinks were not treated. There, the connection of the saddle part to Lagrangian coherent structures based on FTLE is treated. Sadlo and Weiskopf [45] suggested to intersect forward and backward FTLE ridges, which corresponds to half of the constraints in Definition 3. Approaches of this kind, where different time intervals are combined, were criticized by Haller [22], because they are not Lagrangian w.r.t. the total time interval. But as we have seen, the Lagrangian equivalent in Definition 1 is infeasible in practice. Definition 3 bridges the gap between the Lagrangian approach and the FTLE intersection of adjacent intervals [45] providing a categorization that is both Lagrangian and robust.

The closest work w.r.t. sinks is probably by Wiebel et al. [59]. They used the density maximum of particles that were seeded equidistantly in space and repeatedly over time. Up to the exact evaluation of the density maxima, our sink definition is in accordance with theirs because dense particle positions correspond to contracting flowmap behavior. The main difference is that we consider a concrete finite-time interval $[t_0, t_1]$, while they seed repeatedly in time. Their

method can be interpreted as averaging the results of ours over the intervals $[t_i, t_1]$ with $i \in [t_0, t_1]$. They do not consider saddles in their work.

Probably the closest related work overall is by Theisel et al. [53]. In their pathline-based approach, they also categorize pathlines into attractors, repellors, and saddle-like trajectories based on whether their surrounding pathlines converge toward it in forward integration, in backward integration, or both. There are three main differences to our work. First, their approach is local in time. They use the instantaneous orientation of the pathlines in spacetime, which means it cannot encompass the finite-term behavior of the flow. Second for the actual computation, they categorize a point using the Jacobian of the vector field that results from projection of these directions on the plane through spacetime that is orthogonal to the pathline through it. This approach is not objective. Finally, there is no notion of strength or the extraction of representatives, or separatrices.

Our notion of separatrices uses generalized streaklines [61] seeded on the saddles, which is identical to related work on hyperbolic trajectories, saddle core lines, and bifurcation lines [45, 54, 37].

7 Conclusion

We have presented an intuitive Lagrangian extension of the classic 2D vector field critical points saddle, source, and sink to finite-time in Definition 1. It is objective and reflects particle movement in a physically meaningful way. Since it is not robust in practice, we also provide a sufficient criterion in Definition 3 and a first-order approximation for the computation of the category and the strength. We show its independence on changes of the reference frame and point out its relations to existing approaches in the literature.

Looking at the discussion, we do not necessarily consider Definitions 1 and 3 a huge leap over existing methods. We consider the main contribution of this paper to be how this theoretical framework encompasses saddles, sources, sinks, and separatrices and therefore ties together multiple valuable approaches from the literature.

Limitations are that our method is not able to detect all classic critical points, e.g., in linear steady fields because there, the Cauchy Green strain tensor is constant. In addition, just like FTLE, it may detect shear as saddles and may require a high resolution and long computation times for the generation of the flowmap. Furthermore, it loses its ability to capture details in long simulation runs with strong contraction when all particles gather in one point. The categorization is always tied to a given time interval. The same point in space and time could be classified differently for different intervals. In the future, we will analyze strategies to choose meaningful time intervals. Finally, the categorization is undefined at the boundary where particles leave the domain and at the boundary times t_0 and t_1 . Analysis of how the method extends to 3D flow will be future work.

References

1. V. I. Arnold. *Geometrical methods in the theory of ordinary differential equations*, volume 250. Springer Science & Business Media, 2012.
2. D. Asimov. Notes on the Topology of Vector Fields and Flows. Technical Report RNR-93-003, NASA Ames Research Center, 1993.
3. H. Bhatia, V. Pascucci, R. M. Kirby, and P.-T. Bremer. Extracting features from time-dependent vector fields using internal reference frames. In *Computer graphics forum*, volume 33, pages 21–30. Wiley Online Library, 2014.
4. R. Bujack, S. Dutta, I. Baeza Rojo, D. Zhang, and T. Gnther. Objective Finite-Time Saddles and their Connection to FTLE. In J. Johansson, F. Sadlo, and G. E. Marai, editors, *EuroVis 2019 - Short Papers*. The Eurographics Association, 2019.
5. R. Bujack, M. Hlawitschka, and K. I. Joy. Topology-Inspired Galilean Invariant Vector Field Analysis. In *Proceedings of the IEEE Pacific Visualization Symposium, PacificVis 2016 in Taipei, Taiwan*, pages 72–79, 2016.
6. R. Chan. *A Biofluid Dynamic Model for Centrifugal Accelerated Cell Culture Systems*. PhD Dissertation, Leipzig University, Germany, 2008.
7. F. Effenberger and D. Weiskopf. Finding and classifying critical points of 2D vector fields: A cell-oriented approach using group theory. *Computing and Visualization in Science*, 13(8):377–396, Dec. 2010.
8. M. Farazmand and G. Haller. Computing Lagrangian coherent structures from their variational theory. *Chaos: An Interdisciplinary Journal of Nonlinear Science*, 22(1):013128, 2012.
9. M. Farazmand and G. Haller. Attracting and repelling Lagrangian coherent structures from a single computation. *Chaos: An Interdisciplinary Journal of Nonlinear Science*, 23(2):023101, 2013.
10. A. Friederici, T. Günther, C. Rössl, and H. Theisel. Finite Time Steady Vector Field Topology - Theoretical Foundation and 3D Case. In *Vision, Modeling and Visualization*, pages 95–102, 2017.
11. A. Friederici, C. Rössl, and H. Theisel. Finite time steady 2d vector field topology. In *Topological Methods in Data Analysis and Visualization*, pages 253–266. Springer, 2015.
12. G. Froyland. An analytic framework for identifying finite-time coherent sets in time-dependent dynamical systems. *Physica D: Nonlinear Phenomena*, 250:1–19, 2013.
13. R. Fuchs, J. Kemmler, B. Schindler, J. Waser, F. Sadlo, H. Hauser, and R. Peikert. Toward a Lagrangian vector field topology. In *Computer Graphics Forum*, volume 29, pages 1163–1172. Wiley Online Library, 2010.
14. T. Germer, M. Otto, R. Peikert, and H. Theisel. Lagrangian coherent structures with guaranteed material separation. In *Computer Graphics Forum*, volume 30, pages 761–770. Wiley Online Library, 2011.
15. T. Günther, M. Gross, and H. Theisel. Generic objective vortices for flow visualization. *ACM Transactions on Graphics (TOG)*, 36(4):141, 2017.
16. T. Günther, A. Kuhn, and H. Theisel. MCFTLE: Monte Carlo Rendering of Finite-Time Lyapunov Exponent Fields. *Computer Graphics Forum (Proc. EuroVis)*, 35(3):381–390, 2016.
17. T. Günther, M. Schulze, and H. Theisel. Rotation invariant vortices for flow visualization. *IEEE Transactions on Visualization and Computer Graphics (Proc. IEEE Scientific Visualization)*, 22(1):817–826, 2016.

18. T. Günther and H. Theisel. Hyper-objective vortices. *IEEE Transactions on Visualization and Computer Graphics*, 2018.
19. M. Hadwiger, M. Mlejnek, T. Theußl, and P. Rautek. Time-Dependent Flow seen through Approximate Observer Killing Fields. *IEEE Transactions on Visualization and Computer Graphics (Proc. IEEE Scientific Visualization)*, 25(1):1257–1266, Jan 2019.
20. G. Haller. Finding finite-time invariant manifolds in two-dimensional velocity fields. *Chaos: An Interdisciplinary Journal of Nonlinear Science*, 10(1):99–108, 2000.
21. G. Haller. A variational theory of hyperbolic Lagrangian coherent structures. *Physica D: Nonlinear Phenomena*, 240(7):574–598, 2011.
22. G. Haller. Lagrangian coherent structures. *Annual Review of Fluid Mechanics*, 47:137–162, 2015.
23. G. Haller, A. Hadjighasem, M. Farazmand, and F. Huhn. Defining coherent vortices objectively from the vorticity. *Journal of Fluid Mechanics*, 795:136–173, 2016.
24. G. Haller and G. Yuan. Lagrangian coherent structures and mixing in two-dimensional turbulence. *Phys. D*, 147(3-4):352–370, Dec. 2000.
25. C. Heine, H. Leitte, M. Hlawitschka, F. Iuricich, L. De Floriani, G. Scheuermann, H. Hagen, and C. Garth. A survey of topology-based methods in visualization. *Computer Graphics Forum*, 35(3):643–667, 2016.
26. J. L. Helman and L. Hesselink. Representation and display of vector field topology in fluid flow data sets. *Computer*, 22(8):27–36, 1989.
27. J. L. Helman and L. Hesselink. Visualizing Vector Field Topology in Fluid Flows. *IEEE Computer Graphics and Applications*, 11:36–46, 1991.
28. J. C. R. Hunt. Vorticity and vortex dynamics in complex turbulent flows. *Transactions on Canadian Society for Mechanical Engineering (Proc. CANCAM)*, 11(1):21–35, 1987.
29. J. Jeong and F. Hussain. On the Identification of a Vortex. *Journal of Fluid Mechanics*, 285:69–94, 1995.
30. J. Kasten, C. Petz, I. Hotz, B. R. Noack, and H.-C. Hege. Localized finite-time Lyapunov exponent for unsteady flow analysis. In *Vision, Modeling and Visualization*, pages 265–276, 2009.
31. B. Kim and T. Günther. Robust reference frame extraction from unsteady 2D vector fields with convolutional neural networks. *Computer Graphics Forum (Proc. EuroVis)*, page to appear, 2019.
32. G. Kindlmann, C. Chiw, T. Huynh, A. Gyulassy, J. Reppy, and P.-T. Bremer. Rendering and Extracting Extremal Features in 3D Fields. *Computer Graphics Forum*, 37(3):525–536, 2018.
33. A. Kuhn, W. Engelke, C. Rössl, M. Hadwiger, and H. Theisel. Time Line Cell Tracking for the Approximation of Lagrangian Coherent Structures with Subgrid Accuracy. *Computer Graphics Forum*, 33(1):222–234, 2014.
34. J. Kuhnert and S. Sudarshan. Meshfree numerical schemes for time dependent problems in fluid and continuum mechanics. *Advances in PDE modeling and computation*, pages 119–136, 2014.
35. I.-S. Liu. On the transformation property of the deformation gradient under a change of frame. *Journal of elasticity*, 71(1-3):73–80, 2003.
36. H. J. Lugt. The dilemma of defining a vortex. In *Recent developments in theoretical and experimental fluid mechanics*, pages 309–321. Springer, 1979.
37. G. Machado, S. Bobblest, T. Ertl, and F. Sadlo. Space-Time Bifurcation Lines for Extraction of 2D Lagrangian Coherent Structures. *Computer Graphics Forum*, 35(3):91–100, 2016.

38. R. Peikert and M. Roth. The parallel vectors operator: A vector field visualization primitive. In *Proceedings of the Conference on Visualization '99: Celebrating Ten Years*, VIS '99, pages 263–270, Los Alamitos, CA, USA, 1999. IEEE Computer Society Press.
39. A. E. Perry and M. S. Chong. A description of eddying motions and flow patterns using critical-point concepts. *Annual Review of Fluid Mechanics*, 19(1):125–155, 1987.
40. A. Pobitzer, R. Peikert, R. Fuchs, B. Schindler, A. Kuhn, H. Theisel, K. Matkovic, and H. Hauser. The state of the art in topology-based visualization of unsteady flow. *Computer Graphics Forum*, 30(6):1789–1811, 2011.
41. F. H. Post, B. Vrolijk, H. Hauser, R. S. Laramee, and H. Doleisch. The state of the art in flow visualisation: Feature extraction and tracking. *Computer Graphics Forum*, 22(4):775–792, 2003.
42. S. K. Robinson. Coherent motions in the turbulent boundary layer. *Annual Review of Fluid Mechanics*, 23(1):601–639, 1991.
43. M. Roth. *Automatic extraction of vortex core lines and other line type features for scientific visualization*, volume 2. Hartung-Gorre, 2000.
44. M. Roth and R. Peikert. A higher-order method for finding vortex core lines. In *Proceedings of the conference on Visualization'98*, pages 143–150. IEEE Computer Society Press, 1998.
45. F. Sadlo and D. Weiskopf. Time-dependent 2-d vector field topology: An approach inspired by lagrangian coherent structures. In *Computer Graphics Forum*, volume 29, pages 88–100. Wiley Online Library, 2010.
46. J. Sahner, T. Weinkauf, and H.-C. Hege. Galilean invariant extraction and iconic representation of vortex core lines. In *Proc. Eurographics / IEEE VGTC Symposium on Visualization (EuroVis)*, pages 151–160, 2005.
47. J. Sahner, T. Weinkauf, N. Teuber, and H.-C. Hege. Vortex and strain skeletons in eulerian and lagrangian frames. *IEEE Transactions on Visualization and Computer Graphics*, 13(5), 2007.
48. G. Scheuermann, H. Hagen, H. Krüger, M. Menzel, and A. Rockwood. Visualization of higher order singularities in vector fields. In *Proceedings of the 8th conference on Visualization'97*, pages 67–74. IEEE Computer Society Press, 1997.
49. S. C. Shadden, F. Lekien, and J. E. Marsden. Definition and properties of Lagrangian coherent structures from finite-time Lyapunov exponents in two-dimensional aperiodic flows. *Physica D: Nonlinear Phenomena*, 212(3):271–304, 2005.
50. Y. Song. A note on galilean invariants in semi-relativistic electromagnetism. *arXiv preprint arXiv:1304.6804*, 2013.
51. D. Sujudi and R. Haimes. Identification of swirling flow in 3-d vector fields. In *12th Computational Fluid Dynamics Conference*, page 1715, 1995.
52. H. Theisel, T. Weinkauf, H.-C. Hege, and H.-P. Seidel. Saddle connectors - an approach to visualizing the topological skeleton of complex 3D vector fields. In *Proc. IEEE Visualization*, pages 225–232, 2003.
53. H. Theisel, T. Weinkauf, H.-C. Hege, and H.-P. Seidel. Topological methods for 2D time-dependent vector fields based on stream lines and path lines. *Visualization and Computer Graphics, IEEE Transactions on*, 11(4):383–394, July 2005.
54. M. Uffinger, F. Sadlo, and T. Ertl. A Time-Dependent Vector Field Topology Based on Streak Surfaces. *IEEE Transactions on Visualization and Computer Graphics*, 19(3):379–392, March 2013.

55. M. Üffinger, F. Sadlo, M. Kirby, C. D. Hansen, and T. Ertl. FTLE Computation Beyond First-Order Approximation. In *Eurographics (Short Papers)*, pages 61–64, 2012.
56. T. Weinkauf, J. Sahner, H. Theisel, and H.-C. Hege. Cores of swirling particle motion in unsteady flows. *IEEE Transactions on Visualization and Computer Graphics*, 13(6):1759–1766, 2007.
57. T. Weinkauf and H. Theisel. Streak lines as tangent curves of a derived vector field. *IEEE Transactions on Visualization and Computer Graphics*, 16(6):1225–1234, 2010.
58. T. Weinkauf, H. Theisel, K. Shi, H.-C. Hege, and H.-P. Seidel. Extracting higher order critical points and topological simplification of 3D vector fields. In *VIS 05. IEEE Visualization, 2005.*, pages 559–566. IEEE, 2005.
59. A. Wiebel, R. Chan, C. Wolf, A. Robitzki, A. Stevens, and G. Scheuermann. Topological flow structures in a mathematical model for rotation-mediated cell aggregation. In *Topological Methods in Data Analysis and Visualization*, pages 193–204. Springer, 2011.
60. A. Wiebel, C. Garth, and G. Scheuermann. Computation of localized flow for steady and unsteady vector fields and its applications. *IEEE Transactions on Visualization and Computer Graphics*, 1(8), 2002.
61. A. Wiebel, X. Tricoche, D. Schneider, H. Jaenicke, and G. Scheuermann. Generalized streak lines: Analysis and visualization of boundary induced vortices. *IEEE Transactions on Visualization and Computer Graphics*, 13(6):1735–1742, 2007.